Impact of Synthesis Temperature on Morphology, Rheology and Electromagnetic Interference Shielding of CVD-Grown Carbon Nanotube/Polyvinylidene Fluoride Nanocomposites

Seyyed Alireza Mirkhani[a,†], Mohammad Arjmand[a,†], Soheil Sadeghi[a], Beate Krause[b], Petra Pötschke[b], Uttandaraman Sundararaj[a,*]

[a] *Department of Chemical and Petroleum Engineering, University of Calgary, Calgary, Canada*

[b] *Department of Functional Nanocomposites and Blends, Leibniz Institute of Polymer Research Dresden (IPF), Dresden, Germany*

Abstract. Employing chemical vapor deposition technique, multi-walled carbon nanotubes (CNTs) were synthesized over Fe catalyst at a broad range of temperatures, i.e. 550˚C to 950˚C (at 100˚C intervals). CNTs were melt-mixed into a polyvinylidene fluoride (PVDF) matrix at various loadings, and then compression molded. Surprisingly, despite the ascending trend of CNT powder conductivity with the synthesis temperature, the nanocomposites made with CNT synthesized at 650˚C had significantly lower percolation threshold (around 0.4wt%) and higher electromagnetic interference shielding effectiveness (EMI SE) (20.3dB over the X-band for 3.5wt% CNT and 1.1mm thickness) than the other temperatures. Exhaustive characterization studies were conducted on both CNTs and composites to unveil their morphological and electrical characteristics. It is found that superior EMI shielding of $CNT_{650°C}$ was attributed to a combination of high carbon purity, aspect ratio, crystallinity, and powder conductivity along with decent state of dispersion within the PVDF matrix.

1

*Corresponding author. Email: u.sundararaj@ucalgary.ca) (Uttandaraman Sundararaj)

[†] SAM and MA made equal contribution to this work.

1. Introduction

Electromagnetic interference (EMI) shielding is a protection provided to safeguard the performance of electrical and electronic equipment against EMI failure. The EMI shielding market is fueled by growing proliferation of electronics and the subsequent need to reduce the resultant electromagnetic pollution. Moreover, increased environmental issues and health hazardousness owing to EMI have obliged the regulatory bodies to adjust more rigorous EMC standards worldwide.

Metals are the most common materials as EMI shields; nevertheless, compliance issues and environmental concerns over metals disposal coupled with their high density and processing difficulty are currently slowing their growth; this sets to make over the global conductive polymer nanocomposites market as EMI shields. Different types of conductive nanofillers have been employed to develop conductive polymer nanocomposites, viz. carbonaceous nanofillers and metallic nanowires [1, 2], among which carbon nanotube (CNT) has appealed remarkable attention due to its large surface area and excellent electrical and mechanical properties [3].

The EMI shielding of CNT/polymer nanocomposites (CPNs) intensely relies on original physical and geometrical features of CNTs. These features affect the quality of interaction between CNT and polymer matrix, dispersion state of CNT, crystallinity of the polymer matrix, quality of the conductive network, available interacting surface area, and thus the electrical properties of CPNs. The influences of the previously mentioned parameters on the electrical conductivity and EMI shielding of CPNs have been well evaluated in the literature [3-5].

Since the early observation of percolation-dominated electrical conductivity in a CPN by Coleman et al. [6], there have been many papers dedicated to polymer processing and resulting electrical properties of fabricated CPNs. Nevertheless, to the best of our knowledge, there are a rare number of papers correlating the effect of CNT synthesis conditions with the physical characteristics of CNTs, quality of CNT-polymer interaction, and electrical conductivity and EMI shielding of CPNs. We recently investigated the effect of synthesis catalyst on the electrical properties of nitrogen-doped CNT (N-CNT)/polyvinylidene fluoride (PVDF) nanocomposites and showed that N-CNTs synthesized over Co catalyst presented superior EMI shielding compared to Fe and Ni catalysts. This was ascribed to a combination of high carbon purity, high aspect ratio, low nitrogen content and high crystallinity of N-CNTs combined with a good state of N-CNT dispersion [7]. In another study, Krause et al. [8] investigated the impact of synthesis conditions, catalyst,

*Corresponding authors. Email: u.sundararaj@ucalgary.ca (Uttandaraman Sundararaj) and arjmand64@yahoo.com (Mohammad Arjmand)

and solvent on structural properties of CNTs and N-CNTs, and characterized melt-mixed CNT/polyamide 6.6 nanocomposites. They realized that the electrical conductivity of the generated nanocomposites intensely relies on the properties of CNTs, which altered by the synthesis conditions.

This study strives to cover the whole cycle of synthesis-processing-structure-property of CPNs towards EMI shielding applications. The first part of this article is devoted to a detailed characterization of CNTs synthesized at different temperatures using a CVD setup. After that, effects of synthesized carbonaceous fillers on the morphology, rheology, and electrical properties of the developed CPNs, i.e. electrical conductivity, EMI shielding and dielectric properties, are studied. Huge discrepancies between the physical properties of the generated nanofillers and properties of the developed nanocomposites were observed. This provided an in-depth discernment on a correlation between the physical properties of the nanofillers and final properties of the nanocomposites. Moreover, surprisingly, this study revealed an optimum CNT synthesis temperature resulting in CPNs with electrical properties far superior to the other synthesis temperatures.

2. Experimental

2.1. Materials synthesis

Iron (III) nitrate, nonahydrate (Baker Analyzed® ACS Grade) was used as the catalyst precursor in this study. The catalyst was prepared by incipient wetness impregnation of precursor dissolved in distilled water on aluminum oxide support (Sasol Catalox SBa-200). Employing alumina as support offers strong support-metal interaction, facilitating dispersion of metallic particles as well as providing high density of catalyst sites for CNT synthesis [9-11]. In addition, owing to high support-metal interaction, the formation of catalyst particle agglomerates, responsible for the production of graphitic particles and defected CNTs, is heavily reduced. In this study, metal loading over alumina was set to 20wt%. The formed mixture was then dried in two consecutive steps to evaporate water content, i.e. ambient temperature for 24h and 100˚C for 2h.

The catalyst calcination and reduction were carried out in a CVD setup. Description of the apparatus and operation conditions for calcination and reduction of the catalyst can be found elsewhere [12, 13]. X-ray diffraction (XRD) analysis of the catalyst confirmed the formation of iron oxide and metallic iron after calcination and reduction steps, respectively (Figure S1). CNTs were synthesized over the prepared catalyst

*Corresponding authors. Email: u.sundararaj@ucalgary.ca (Uttandaraman Sundararaj) and arjmand64@yahoo.com (Mohammad Arjmand)

at a broad spectrum of temperatures, i.e. 550°C to 950°C (at 100°C intervals). The synthesis time and catalyst mass were fixed at 2h and 0.6g, respectively. The gas flow rates were 50/50/50sccm for ethane/argon/hydrogen.

The polymer matrix used for the nanocomposite preparation was a semi-crystalline polyvinylidene fluoride (PVDF) 11008/0001, purchased from 3M Canada, with an average density of 1.78g/cm^3 and melting point of 160°C. PVDF was selected as the polymer matrix owing to its ferroelectricity, high dielectric strength ($\sim$ 13kV·mm^{-1}), corrosion resistance and robust interaction of electrophilic fluorine groups with CNTs [14-17]. APAM (Alberta Polymer Asymmetric Minimixer) was used to melt-mix CNTs with the PVDF matrix at 240°C and 235rpm. The PVDF matrix was first masticated within the mixing cup for 3min, and then CNTs were inserted and mixed for an extra 14min. For each CNT synthesis temperature, nanocomposites with different CNT concentrations, i.e. 0.3, 0.5, 1.0, 2.0, 2.7 and 3.5wt%, were prepared. Nanocomposites were molded into rectangular (1.1mm thickness) and circular (0.5mm thickness) cavities with a Carver compression molder (Carver Inc., Wabash, IN) at 220°C under 38MPa pressure for 10min. The rectangular samples were used for conductivity and EMI shielding characterizations, whereas the circular samples were employed for rheological characterizations.

2.2. Materials characterization

2.2.1 Catalyst and CNT characterization

BET of catalyst: The Brunauer-Emmett-Teller (BET) method was used to measure the surface area of the catalysts. We exposed the reduced catalysts to the various CNT synthesis temperatures for 5min in the reactor to verify the impact of synthesis temperature on the sintering of the catalysts. This was performed by comparing the available surface area of the catalyst-free alumina substrate (as-received) and catalyst-loaded alumina substrate exposed to the synthesis temperatures. BET of the catalysts was performed using an Autosorb-1, Quantachrome Instruments, USA. This set up works based on the adsorption of N_2 at the temperature of liquid nitrogen (77K). Prior to the measurements, all samples were degassed under vacuum at 353K for 3h.

Thermogravimetric analysis: The carbon purity and the thermal stability of CNTs were examined with a Thermogravimetric Analyzer (TA Instruments, Model: Q500). The samples were heated under air

*Corresponding authors. Email: u.sundararaj@ucalgary.ca (Uttandaraman Sundararaj) and arjmand64@yahoo.com (Mohammad Arjmand)

atmosphere (Praxair AI INDK) from room temperature to 900°C at a rate of 10°C/min. The samples were kept at 950°C for 10min before cooling.

Scanning and transmission electron microscopy of CNTs: High-resolution scanning and transmission electron microscopy (HRSEM and HRTEM) was used to investigate the morphology of synthesized CNTs. A high-resolution Philips XL30 was used to obtain SEM images. HRTEM was performed on a Tecnai TF20 G2 FEG-TEM (FEI, Hillsboro, Oregon, USA) at 200kV acceleration voltage with a standard single-tilt holder. The images were captured with a Gatan UltraScan 4000 CCD camera (Gatan, Pleasanton, California, USA) at 2048 × 2048 pixels. For the HRTEM, less than 1.0mg of the CNT powder was suspended in 10mL ethanol and bath sonicated for 15min. A drop of the suspension was mounted on the carbon side of a standard TEM grid covered with a ~ 40nm holey carbon film (EMS, Hatfield, Pennsylvania, USA). Measurement of the geometrical dimensions of CNTs was performed for more than 150 individual ones using the MeasureIT software (Olympus Soft Imaging Solutions GmbH).

Conductivity of CNT powder: The electrical conductivity of CNT powders was measured using an especially designed instrument. The powder of 40–50mg was filled into a cylinder and compressed by a piston, and then the electrical resistance of the powder was measured using a Keithley 2001 electrometer. The powder conductivity was measured at various piston pressures, i.e. 5, 10, 20, 25, and 30MPa. Further details on this procedure are provided elsewhere [18].

2.2.2. Nanocomposite characterization

CNT dispersion: The state of CNT dispersion in the PVDF matrix was studied in two scales: microdispersion and nanodispersion. The microdispersion state of CNTs within the PVDF matrix was quantified using light transmission microscopy (LM) on thin cuts (5µm thickness) of the compression-molded samples, prepared with a Leica microtome RM2265 (Leica Microsystems GmbH, Wetzlar, Germany) equipped with a diamond knife. An Olympus microscope BH2 equipped with a CCD camera DP71 (both from Olympus Deutschland GmbH, Hamburg, Germany) connected to the software Stream Motion (Olympus) was used to take images with dimensions of $600 \times 800 \mu m^2$ from different cut sections. The software Stream Motion (Olympus) was used to analyze the images. The agglomerate area ratio (in %) was defined by dividing the detected area of non-dispersed nanofillers (with an equivalent circle diameter > 5µm, Area > $19.6\mu m^2$) over the whole sample area (15 cuts, ca. $7.2mm^2$). Mean value and standard

*Corresponding authors. Email: u.sundararaj@ucalgary.ca (Uttandaraman Sundararaj) and arjmand64@yahoo.com (Mohammad Arjmand)

deviation, demonstrating the discrepancies between the cuts and thus heterogeneity, were reckoned. The relative transparency of the cuts provided added information about the amount of dispersed nanofillers in the samples. The relative transparency was quantified by dividing the transparency of the cut over the transparency of the glass slide/cover glass assembly. Ten various areas per sample were used to obtain mean values and standard deviations. Further information on using LM to evaluate microdispersion state of nanofillers within the nanocomposites is presented elsewhere [7, 19, 20]. For the nanodispersion, ultrathin sections (60nm) of the samples were cut using an ultramicrotome EM UC6/FC6 (Leica, Austria) with an ultrasonic diamond knife at room temperature. The sections were then transferred onto carbon-filmed TEM copper grids. TEM observations were performed using TEM LIBRA 120 (Carl Zeiss SMT, Oberkochen, Germany) with an acceleration voltage of 120kV.

Rheology: Rheological measurements were performed using an Anton-Paar MCR 302 rheometer at 240 ± 0.5°C using 25mm cone-plate geometry with a cone angle of 1° and truncation of 47μm. Large amplitude oscillatory shear response of neat PVDF and CNT/PVDF nanocomposites was obtained to characterize the origin of nonlinearities and to better understand morphologies formed by the nanofillers.

Electrical conductivity: Two conductivity meters with 90V as the applied voltage were employed to measure the DC electrical conductivity of the generated materials. For the nanocomposites with an electrical conductivity higher than 10^{-2}S·m^{-1}, the measurements were conducted according to the ASTM 257-75 standards using a Loresta GP resistivity meter (MCP-T610 model, Mitsubishi Chemical Co., Japan) connected to an ESP probe. For electrical conductivities less than 10^{-2}S·m^{-1}, the measurements were performed with a Keithley 6517A electrometer connected to a Keithley 8009 test fixture (Keithley instruments, USA).

EMI shielding and dielectric properties: EMI shielding measurements over the X-band frequency range (8.2-12.4GHz) were performed using an E5071C network analyzer (ENA series 300KHz - 20GHz). In order to perform the measurements, the samples were sandwiched between two waveguides of the network analyzer. The network analyzer sent a signal down the waveguide incident to the sample and then the scattering parameters (S-parameters) of each sample were recorded and used to measure EMI shielding effectiveness (EMI SE). EMI SE is expressed in dB and is the logarithm of the ratio of the incident power to the transmitted power. The dielectric properties of the made nanocomposites over the X-band were also achieved by S-parameters conversion using Reflection/Transmission Mu and Epsilon Nicolson-Ross Model [21, 22].

*Corresponding authors. Email: u.sundararaj@ucalgary.ca (Uttandaraman Sundararaj) and arjmand64@yahoo.com (Mohammad Arjmand)

*Corresponding authors. Email: u.sundararaj@ucalgary.ca (Uttandaraman Sundararaj) and arjmand64@yahoo.com (Mohammad Arjmand)

3. Results and Discussion

3.1. Characterization of catalysts and CNTs

Table 1 presents the BET surface area of the reduced catalysts exposed to the investigated synthesis temperatures for a short period. The surface area for pure alumina support (as-received) was measured to be 207m²/g; nevertheless, the measured surface area of the catalyst-loaded alumina exposed to the synthesis temperatures was much lower than pure alumina, indicating high loading of iron nanoparticles. It was interestingly observed that the surface area of the loaded alumina had a descending trend with the synthesis temperature. For instance, surface area of loaded alumina at 950°C showed 34% reduction compared to 550°C. This reduction can be ascribed to the blockage of alumina pores due to sintering of iron nanoparticles at high temperatures. Therefore, it can be claimed that the catalyst nanoparticles underwent intense sintering at high synthesis temperatures.

Table 1: BET surface area of reduced catalysts exposed to various synthesis temperatures for a short period.

Sample	BET Surface Area [m^2/g]
As-received Alumina	207.0
Reduced Catalyst (550°C)	140.5
Reduced Catalyst (650°C)	135.7
Reduced Catalyst (750°C)	123.2
Reduced Catalyst (850°C)	108.5
Reduced Catalyst (950°C)	92.3

Employing TG analysis, we obtained valuable information about thermal stability, carbon purity, and quality of synthesized CNTs. The first derivative of TG (DTG) also determines the nature of carbonaceous material decomposition, which can take place in single or multiple mass-loss stages. Figure 1 depicts TG and DTG graphs of CNTs synthesized at various temperatures and Table 2 presents the thermal features of synthesized CNTs. In the TG analysis, synthesized carbonaceous materials degraded and remaining residue consisted of catalyst particles; accordingly, the amount of degraded material denotes the carbon purity.

*Corresponding authors. Email: u.sundararaj@ucalgary.ca (Uttandaraman Sundararaj) and arjmand64@yahoo.com (Mohammad Arjmand)

As shown in Figure 1(a) and tabulated in Table 2, $CNT_{550°C}$ showed by far the lowest carbon purity of 43.1% and $CNT_{650°C}$ presented the highest carbon purity of 85.4%. Carbonaceous fillers synthesized at the other three temperatures presented carbon purity around 70%. In this regard, 650°C stands out in terms of carbon purity. These results were also qualitatively confirmed with the XRD of CNTs (Figure S2). We believe that the inferior carbon purity at 550°C is due to low synthesis temperature, whereas lower carbon purities at 750°C and higher temperatures are owing to the sintering of catalyst nanoparticles. The catalyst particles comprised 80wt% alumina and 20wt% metallic particles. Alumina is insulative and metallic particles have much lower surface area than synthesized CNTs, and their surface area reduced further due to sintering phenomenon at the synthesis temperatures. This explains why low carbon purity can drastically deteriorate the electrical properties and confirms the significance of carbon purity on the final electrical properties.

Figure 1(b) shows that $CNT_{550°C}$ depicts a much broader DTG curve than CNTs synthesized at the other temperatures. Moreover, the onset degradation point for $CNT_{550°C}$ is much lower than the other types of CNTs. This can be ascribed to low synthesis temperature, facilitating the formation of amorphous carbon or defective CNTs [6]. $CNT_{650°C}$ and $CNT_{750°C}$ presented narrow DTG curves, implying the superior quality of CNTs.

It was surprisingly observed that $CNT_{850°C}$ and $CNT_{950°C}$ indicated a very different shape of DTG curve compared to the other three temperatures. The shaded box presents the portion of carbonaceous fillers synthesized at 850°C and 950°C made of CNTs. The left side of the shaded box coincides with the initiation of the degradation of $CNT_{850°C}$ and $CNT_{950°C}$, which is far higher than the other synthesis temperatures. The high onset degradation points for 850°C and 950°C, listed in Table 2, show that no thermally weak materials formed at these two synthesis temperatures, and the crystallinity of synthesized CNTs at 850°C and 950°C was superior to the other synthesis temperatures. The right side of the shaded box signifies the temperature at which CNTs were fully decomposed, matching the plateau in the TG curves of $CNT_{550°C}$, $CNT_{650°C}$, and $CNT_{750°C}$. We think that the portion of the TG curves of the samples produced at 850°C and 950°C located at the right side of the shaded box belongs to highly thermal-resistant conductive carbonaceous materials, as will be later confirmed by compressed powder conductivity data, SEM and TEM. Hence, it can be asserted that the final material synthesized at 850°C and 950°C comprised a thermal-resistant carbonaceous material, CNT and catalyst. We think that the thermal-resistant carbonaceous material synthesized at high temperatures arose from sintering and coalescence of catalyst particles, leading to the coverage of large

*Corresponding authors. Email: u.sundararaj@ucalgary.ca (Uttandaraman Sundararaj) and arjmand64@yahoo.com (Mohammad Arjmand)

catalyst particles by the carbonaceous materials. We will endorse this speculation by scanning and transmission electron microscopy.
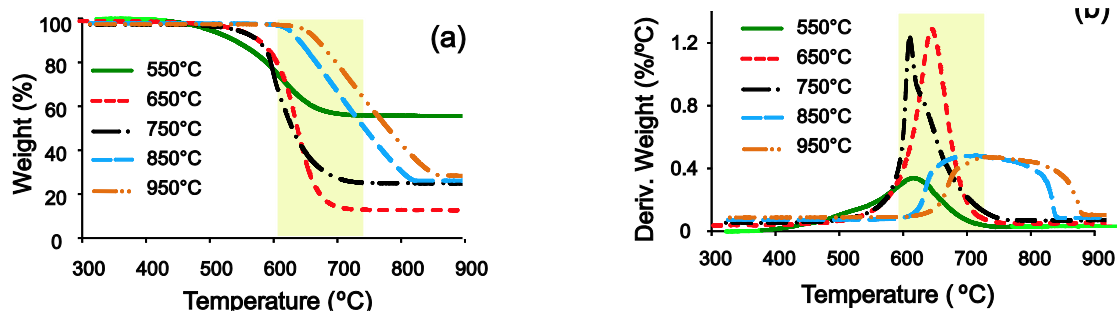

Figure 1: (a) TG and (b) DTG graphs of CNTs synthesized at various temperatures.

Table 2: Thermal features of CNTs synthesized at different temperatures.

Synthesis Temperature	550˚C	650˚C	750˚C	850˚C	950˚C
Onset Point (˚C)	522	575	581	622	652
Inflection Point (˚C)	612	636	599	696	711
Synthesis Yield %	43.1	85.4	72.7	71.1	68.7

Figure 2 depicts the SEM micrographs of CNT powders. SEM reveals that synthesis temperature had a tremendous impact on the morphology of synthesized CNTs. As shown in Figure 2, the micrograph of $CNT_{550˚C}$ shows the highest density of catalyst particles among all samples (yellow arrows), covered by small-diameter CNTs; this is in accord with low carbon purity for 550˚C. The micrographs for $CNT_{650˚C}$ and $CNT_{750˚C}$ reveal the rich formation of entangled low-diameter CNTs over the catalyst particles.

*Corresponding authors. Email: u.sundararaj@ucalgary.ca (Uttandaraman Sundararaj) and arjmand64@yahoo.com (Mohammad Arjmand)
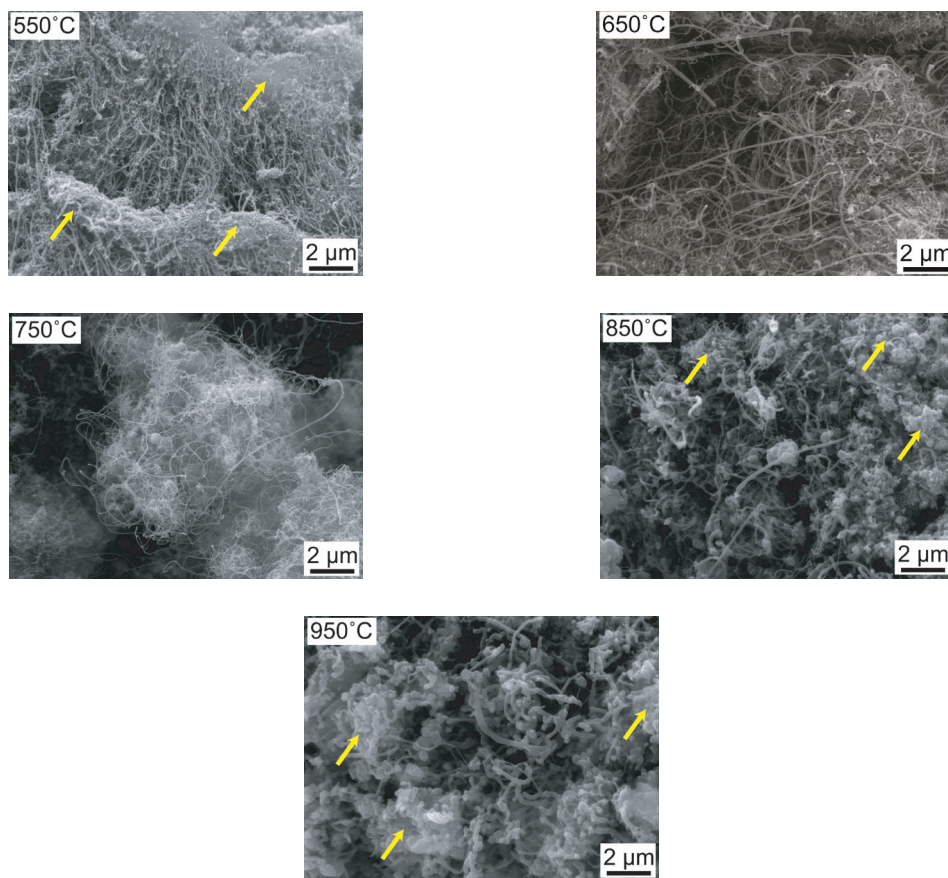
Figure 2: SEM micrographs of CNT powders synthesized at various temperatures.

At higher synthesis temperatures (850°C and 950°C), CNTs with much larger diameters compared to lower synthesis temperatures are observable. This is attributable to sintering of catalyst particles at higher temperatures. The possibility of more intense sintering of catalyst particles at 850°C and 950°C was already validated by low BET surface of catalyst samples, denoting iron catalyst particles agglomeration. SEM micrographs of 850°C and 950°C also indicate the formation of thermal-resistant carbonaceous materials on the surface of large catalyst particle clusters (yellow arrows). This was endorsed by TG analysis, TEM images (Figure S3) and Raman spectroscopy of CNTs (Figures S4).

Employing TEM images (Figure S3), we obtained the average diameter and length of CNTs synthesized at 550°C, 650°C, and 750°C for around 150 individual CNTs (Figure 3(a)). It is worth noting that

*Corresponding authors. Email: u.sundararaj@ucalgary.ca (Uttandaraman Sundararaj) and arjmand64@yahoo.com (Mohammad Arjmand)

synthesized CNTs presented a wide range of length and diameter, as depicted in Figure S5. These results are of high importance since CPNs fabricated from CNTs with large length and small diameter have superior electrical performance [23, 24]. It should be mentioned that we could not find sufficient number of individual CNTs at 850˚C and 950˚C using TEM images to launch the statistical analysis of length and diameter. This is due to sintering of catalyst at high temperatures, hindering the formation of CNTs. Nevertheless, it is vivid in the SEM images that the diameters of formed CNTs at 850˚C and 950˚C are larger than the other types of CNTs. Figure 3(a) shows that $CNT_{650°C}$ presented an average diameter of 14.7nm, which is lower than $CNT_{550°C}$ and $CNT_{750°C}$. The results also indicate that the length of CNTs synthesized at 650˚C was around 0.7µm, which is almost half of the length of CNTs synthesized at 550˚C and 750˚C (~1.3µm).

Figure 3(b) shows the powder conductivity of synthesized fillers as a function of piston pressure (up to 30 MPa). As expected, powder conductivity showed a slight ascending trend with pressure, due to increased contact area between individual fillers at higher pressures. More importantly, it was observed that the powder conductivity presented an ascending trend with the synthesis temperature. For instance, at 30 MPa, $CNT_{550°C}$, $CNT_{650°C}$ and $CNT_{950°C}$ showed powder conductivity of 1090, 1760 and 4030 S·m^{-1}, respectively. The ascending trend of powder conductivity with the synthesis temperature can be related to superior crystalline structures formed at high temperatures.
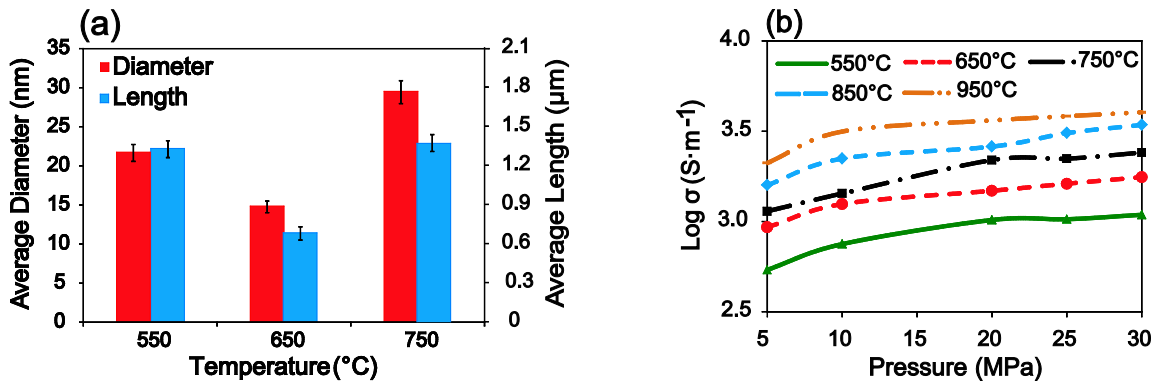

Figure 3: (a) Average length and diameter of CNTs synthesized at 550˚C, 650˚C, and 750˚C. (b) Conductivity of compressed powders of CNTs synthesized at various temperatures.

*Corresponding authors. Email: u.sundararaj@ucalgary.ca (Uttandaraman Sundararaj) and arjmand64@yahoo.com (Mohammad Arjmand)

Raman spectroscopy is a powerful tool to distinguish different allotropes of carbon. There are two main characteristic peaks for Raman spectroscopy of CNTs:

- D-band, observed around 1350cm^{-1} and attributed to the disorders / defects in the structure of CNTs, as well as presence of amorphous carbon [25].

- G-band, which corresponds to tangential vibrations of the graphitic carbon atoms. This band occurs around 1580-1590cm^{-1}. Unlike D-band, this band can occur in all sp^2 sites.

One of the important features that can be derived from Raman data is the D-band to G-band intensity ratio, I_D/I_G, which reflects defect intensity of synthesized CNTs. In fact, I_D/I_G can be used as a useful measure to investigate the crystallinity of CNTs synthesized at various temperatures. We spotted 25 different points in the samples to obtain reliable results from the Raman spectra of synthesized CNTs. Typical Raman spectrum observed for our synthesized CNTs can be viewed in Figure S4.

For the sake of ratio calculation, as suggested by Ferrari and Robertson [25], D-band and G-band data were fitted by Lorentzian and Breit-Wigner-Fano (BWF) functions, respectively. Then the area of the fitted peaks was considered to calculate I_D/I_G. As can be seen in Figure 4, the highest values of I_D/I_G of about 1.6 were observed for CNT$_{850}$ and CNT$_{950°C}$, which is most likely due to formation of thermal-resistant carbonaceous material on the surface of sintered catalyst. For CNTs synthesized at 550°C, 650°C and 750°C, we obtained much lower I_D/I_G value of about 0.8, indicating that at these temperatures mostly CNTs formed rather than thermal-resistant carbonaceous material. This result matches closely with the TEM images and TGA results.

*Corresponding authors. Email: u.sundararaj@ucalgary.ca (Uttandaraman Sundararaj) and arjmand64@yahoo.com (Mohammad Arjmand)
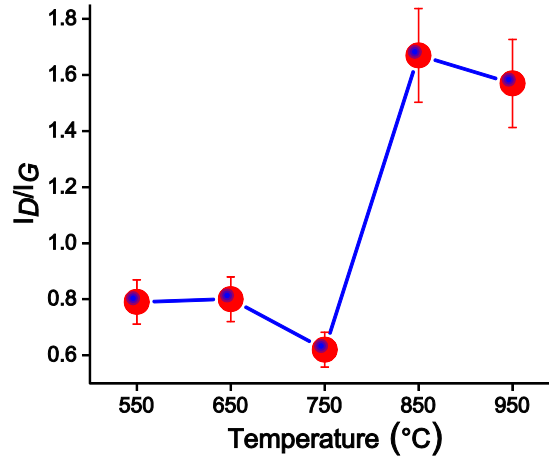
Figure 4: Intensity ratios of *D*-band and *G*-band for synthesized CNTs.

3.2 Characterization of nanocomposite

3.2.1. LM and TEM

Transmission light microscopy (LM) was used to characterize the state of microdispersion in nanocomposite samples. LM images of samples with 2.0wt% of CNTs are compared in Figure 5. The images differ in their part of nanotubes that still exists as agglomerates and could not be dispersed under the selected mixing conditions. This non-dispersed part, as quantified using the agglomerate area ratio (Table 3), is the lowest for $CNT_{650°C}$, illustrating that this kind of CNTs was dispersed best. It was interesting to observe that $CNT_{750°C}$ showed the highest amount of large agglomerate.

In addition, the gray appearance of the LM image background was analyzed as it reflects the number of agglomerates with sizes equal to or slightly larger than the wavelength of visible light (ca. 400-700nm) but smaller than visually detectable agglomerates. The more nanotubes are dispersed in this size range, the darker the background appears. The lowest relative transparency is also seen for the sample with $CNT_{650°C}$, appearing much darker than all other samples. This can be attributed to high carbon purity and high aspect ratio of $CNT_{650°C}$. For nanocomposites containing $CNT_{850°C}$ and $CNT_{950°C}$, the highest transparencies were detected at 86.9% and 90.6%, respectively. It can be concluded that only a very low amount of fillers was dispersed in these nanocomposites and the main part for CNTs is located in agglomerates. We relate this to

*Corresponding authors. Email: u.sundararaj@ucalgary.ca (Uttandaraman Sundararaj) and arjmand64@yahoo.com (Mohammad Arjmand)

the formation of a large amount of thermal-resistant carbonaceous material on the surface of sintered catalysts, having much less surface area compared to CNTs.

*Corresponding authors. Email: u.sundararaj@ucalgary.ca (Uttandaraman Sundararaj) and arjmand64@yahoo.com (Mohammad Arjmand)
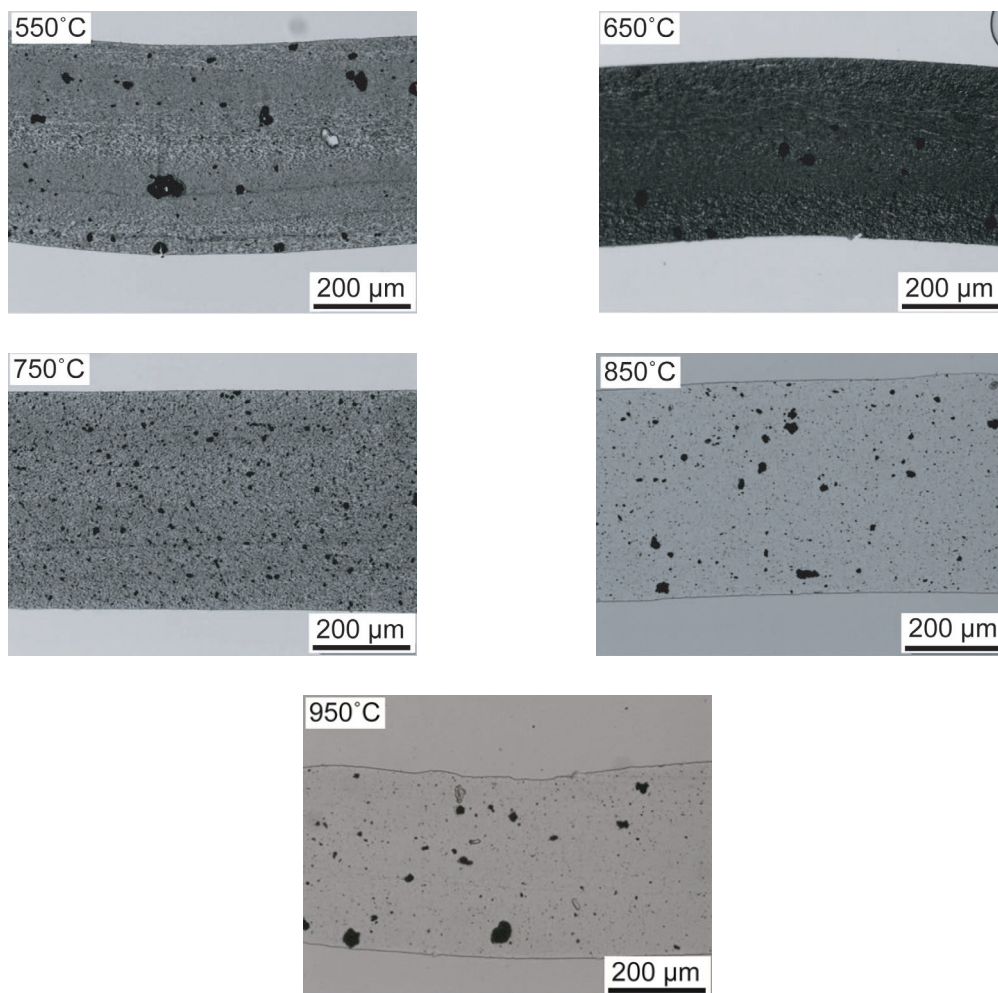
Figure 5: LM images of microtomed CNT/PVDF nanocomposite.

Table 3: Agglomerate area ratio and relative transparency of thin cuts of 2.0wt% CNT/PVDF nanocomposites.

Synthesis Temperature	550°C	650°C	750°C	850°C	950°C
Agglomerate Area Ratio %	3.2	0.8	4.7	2.7	1.9
Relative Transparency %	45.0	23.3	46.2	86.9	90.6

*Corresponding authors. Email: u.sundararaj@ucalgary.ca (Uttandaraman Sundararaj) and arjmand64@yahoo.com (Mohammad Arjmand)

TEM was used to characterize agglomerate sizes below the LM limit, and it shows the state of nanodispersion, wherein individually dispersed nanotube can be detected (Figure 6). It is clearly seen that the nanocomposites with $CNT_{850°C}$ and $CNT_{950°C}$ show the worst nanodispersion. Nearly no individualized nanotubes can be observed next to very large agglomerates. The best nanodispersion state of nanotubes was achieved for $CNT_{650°C}$, whereas in the case of $CNT_{550°C}$, small agglomerates are detected. In brief, the LM images coupled with TEM images vividly illustrate that the CNT material produced at 650°C shows the best and $CNT_{850°C}$ and $CNT_{950°C}$ indicate the worst dispersibility at both microscale and nanoscale.
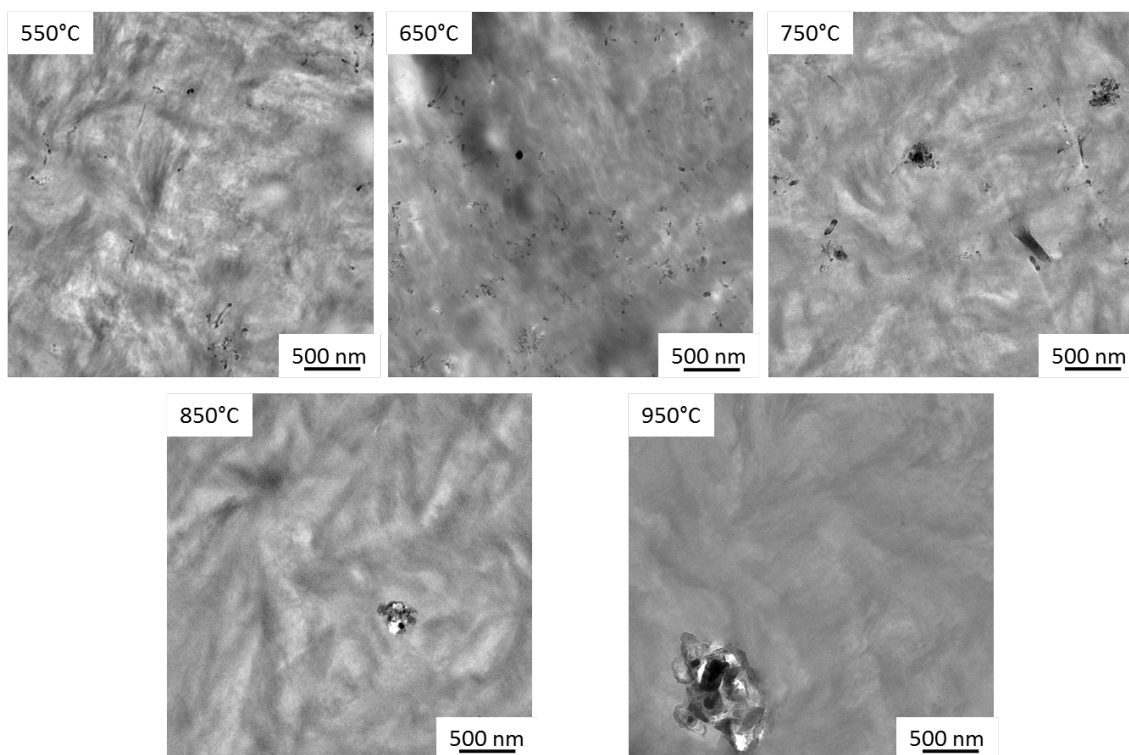

Figure 6: TEM images of CNT/PVDF nanocomposites.

It is known that the matrix crystallinity may influence the composite's electrical properties [26]. Differential scanning calorimetry (DSC) revealed that the overall crystallinity increased only slightly from 49.5% for pure PVDF to max. 53.5% for $CNT_{750°C}$ (Figure S6). The results illustrate that possible changes in the electrical behavior were not due to different PVDF matrix crystallinity.

*Corresponding authors. Email: u.sundararaj@ucalgary.ca (Uttandaraman Sundararaj) and arjmand64@yahoo.com (Mohammad Arjmand)

*Corresponding authors. Email: u.sundararaj@ucalgary.ca (Uttandaraman Sundararaj) and arjmand64@yahoo.com (Mohammad Arjmand)

3.2.2. Rheometry

Figure 7 depicts oscillatory amplitude sweep response of neat PVDF and CNT/PVDF nanocomposites containing 2.7wt% of carbon nanotubes synthesized at different temperatures over a wide range of applied strain amplitudes from 0.1 to 1000.0% at an angular frequency of 10rad/s. As strain amplitude increases, the responses observed for neat PVDF and CNT/PVDF nanocomposite samples feature a drop in G' and a transition from a linear regime to a nonlinear regime. It is noticeable that in the low-strain region, all nanocomposite samples exhibited a solid-like response ($G' > G''$) except for the $CNT_{750°C}$/PVDF sample, the sample with highest agglomerate area ratio. In addition, all nanocomposite samples, except for $CNT_{650°C}$/PVDF, showed a multi-step transition into a nonlinear regime as G' dropped to an intermediate plateau and then significantly decreased. Interestingly, for nanocomposites with a multi-step transition, the first-step decrease in G' was accompanied by a dissipation process, signified by a local peak in G''.

The oscillatory amplitude sweep response observed for $CNT_{650°C}$/PVDF sample corresponds to a single-yielding process occurred by *stochastic erosion* [27, 28] of a highly flocculated gelled structure formed by carbon nanotubes, bound polymer chains and matrix entanglement network. In contrary, $CNT_{750°C}$/PVDF sample demonstrated a weak initial drop in G' at strain amplitudes of ~O (1%), followed by a significant decrease in the elastic response at larger strain amplitudes (see the inset). Similarly, $CNT_{550°C}$/PVDF, $CNT_{850°C}$/PVDF and $CNT_{950°C}$/PVDF samples showed a distinct initial drop in G' to an intermediate plateau, followed by a second transition at larger strain amplitudes.

Multi-step yielding process has been previously reported for a variety of colloidal systems such as depletion-induced gels [29, 30], nano-emulsions [31], glassy micro-gels [32], magnetorheological suspensions [33], and high concentration attractive glasses [29, 30]. Several mechanisms have been proposed as the cause of a multi-step transition from a solid-like behavior into a fluid-like behavior. This process has been mainly attributed to the escape of particles from the potential well of their nearest neighbor, followed by agglomerated structures disintegration at larger strains. In addition to microstructural changes under intermediate/large strain amplitudes, non-idealities, flow heterogeneities and instabilities might have some impacts on flow kinematics and the observed response [34, 35].

Observing a single-step transition from a solid-like state into a fluid-like state for $CNT_{650°C}$/PVDF nanocomposite can be interpreted in terms of irreversible decrease in number of load-bearing network junctions formed by direct tube-tube contact as oscillatory strain amplitude increases [36]. Whilst, the

*Corresponding authors. Email: u.sundararaj@ucalgary.ca (Uttandaraman Sundararaj) and arjmand64@yahoo.com (Mohammad Arjmand)

multi-step yielding transition observed for $CNT_{550°C}$/PVDF, $CNT_{750°C}$/PVDF, $CNT_{850°C}$/PVDF and $CNT_{950°C}$/PVDF nanocomposites signifies a fundamental difference in the origin of their solid-like behavior under small strain amplitudes and their fluidization as strain amplitude increases compared to $CNT_{650°C}$/PVDF nanocomposite. In fact, solid-like behavior and elasticity at small strain amplitudes in nanocomposite samples, except for $CNT_{650°C}$/PVDF sample, could be mainly due to inter-agglomerate links [37]. In other words, intra-agglomerate links are much stronger than those formed by inter-agglomerate contacts. This could be also due to poor wettability of agglomerates constituents by the polymer melt, leading to a poor stress transfer across the polymer-agglomerate interface. This implies that structural failure in $CNT_{550°C}$/PVDF, $CNT_{750°C}$/PVDF, $CNT_{850°C}$/PVDF and $CNT_{950°C}$/PVDF nanocomposites commenced by breakage of agglomerate-agglomerate links at intermediate strain amplitudes, followed by widespread network bonds rupture and disintegration of agglomerates [38].
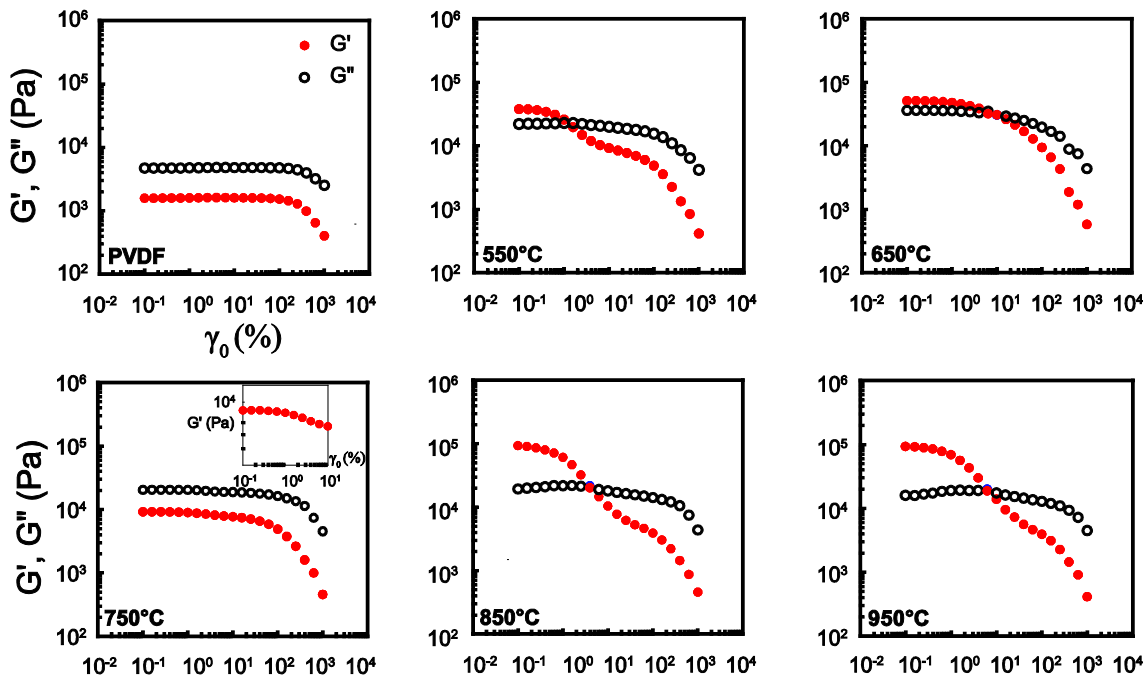

Figure 7: Oscillatory amplitude sweep response of neat PVDF and CNT/PVDF nanocomposites containing 2.7wt% of carbon nanotubes synthesized at different temperatures for strain amplitudes of γ_0=0.1-1000% at an angular frequency of ω =10rad/s. The inset shows magnified response of $(CNT)_{750°C}$/PVDF for strain amplitudes of 0.1-10.0%.

*Corresponding authors. Email: u.sundararaj@ucalgary.ca (Uttandaraman Sundararaj) and arjmand64@yahoo.com (Mohammad Arjmand)

As previously mentioned, for nanocomposites with a multi-step transition into the nonlinear regime, the initial drop in G' was accompanied by a dissipation process marked by a peak in G''. This dissipation event can be attributed to structural reorganization induced by failure of inter-agglomerate links under intermediate strain amplitudes. Densification of agglomerates by drainage of interstitial fluid could also have a contribution to these observations. This hypothesis is consistent with our light microscopy observations for the microdispersion state of CNTs in the PVDF matrix. The low relative transparency observed for $CNT_{750°C}$/PVDF nanocomposite implied the presence of well-dispersed CNT clusters, 400-700nm or slightly larger in size, in this sample. Furthermore, observing relatively high agglomerate area ratio for $CNT_{750°C}$/PVDF nanocomposite confirms the presence of poorly dispersed CNT domains (see Table 3 for details). This dual response could be attributed to lower carbon purity achieved at 750°C compared to 650°C. In analogy, in $CNT_{550°C}$/PVDF nanocomposite, very low CNT carbon purity (~43.1%) led to a major contribution from non-CNT constituents to the rheological response, mainly controlled by inter-agglomerate links rigidity. Similar scenario could be applicable to the observed nonlinear response of $CNT_{850°C}$/PVDF and $CNT_{950°C}$/PVDF nanocomposites. High relative transparencies observed for these nanocomposites indicate the presence of very rigid agglomerates in these samples that coupled with a poor stress transfer across polymer-agglomerate interface, leading to flow-induced structural failure initiated from agglomerate boundaries.

3.2.3. Electrical conductivity and EMI shielding

High electrical conductivity is a prerequisite for acceptable EMI shielding [39]. Accordingly, conductivity profile of nanocomposite samples was studied as a function of CNT content, as shown in Figure 8(a). It is observed that the synthesis temperature had a tremendous impact on the electrical conductivity of the generated nanocomposites. $CNT_{650°C}$ nanocomposites showed electrical conductivity and percolation threshold far superior to the other temperatures. Moreover, contrary to the ascending trend of the powder conductivity with the synthesis temperature, it was interestingly observed that the nanocomposites made with $CNT_{850°C}$ and $CNT_{950°C}$ demonstrated an insulative behavior spanning the whole concentration range.

Employing the statistical percolation theory [40, 41], $CNT_{650°C}$ nanocomposites presented a percolation threshold equal to 0.4wt%, whereas $CNT_{550°C}$ and $CNT_{750°C}$ nanocomposites presented percolation

*Corresponding authors. Email: u.sundararaj@ucalgary.ca (Uttandaraman Sundararaj) and
arjmand64@yahoo.com (Mohammad Arjmand)

thresholds of 1.0wt% and 2.3wt%, respectively. The percolation threshold obtained for $CNT_{650°C}$ nanocomposites is comparable to or lower than the results presented for CNT/PVDF nanocomposites in the literature [42-44]. It was also observed that the maximum conductivity obtained for $CNT_{650°C}$ nanocomposites was much higher than the other temperatures. The maximum conductivities for $CNT_{550°C}$, $CNT_{650°C}$, and $CNT_{750°C}$ nanocomposites at 3.5wt% were 0.4, 31.2, and 0.1S·m^{-1}, respectively. The maximum conductivities of the nanocomposites were fairly lower than the conductivities obtained for the compressed powders. This is due to the presence of polymer layers between CNTs in CPNs, highlighting the role of tunneling and hopping mechanisms rather than the direct-contact mechanism [45, 46].
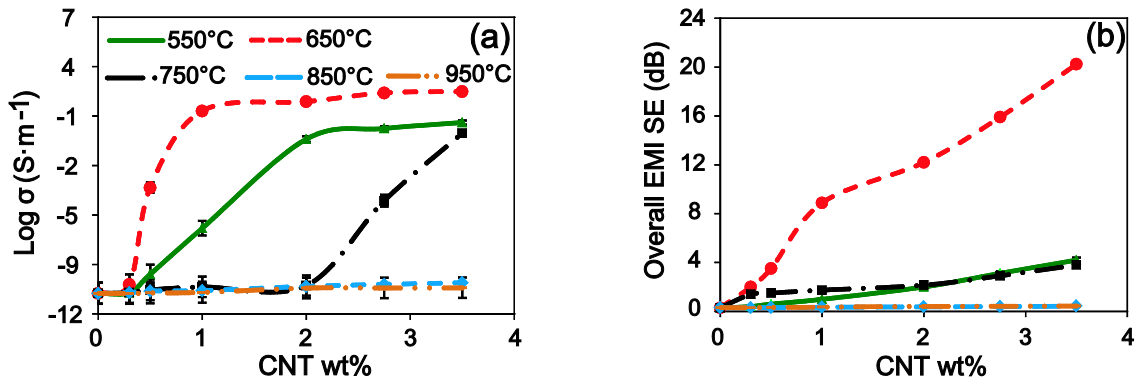

Figure 8: (a) Electrical conductivity and (b) EMI SE of CNT/PVDF nanocomposites made at different synthesis temperatures as a function of CNT content.

The insulative nature of $CNT_{850°C}$ and $CNT_{950°C}$ nanocomposites was due to lack of the formation of conductive network at these two temperatures. As confirmed by TGA, powder conductivity, SEM and TEM, a huge amount of conductive carbonaceous structures was formed around the sintered catalyst particles at these two temperatures. Furthermore, CNTs synthesized at these two temperatures had higher diameter compared to the other synthesis temperatures, and carbon purity indicated an intermediate value. These all led to lack of the formation of conductive network within the PVDF matrix for these two temperatures, despite their high powder conductivity. According to the excluded volume and statistical percolation theories [3, 40, 47, 48], spherical particles have much higher percolation threshold than cylindrical particles, and percolation threshold scales inversely with the aspect ratio of cylinders. This

*Corresponding authors. Email: u.sundararaj@ucalgary.ca (Uttandaraman Sundararaj) and arjmand64@yahoo.com (Mohammad Arjmand)

justifies why large-diameter CNTs and carbonaceous materials formed on the surface of catalyst clusters at 850°C and 950°C could not form any conductive network.

The observed discrepancies in the percolation curves of $CNT_{550°C}$, $CNT_{650°C}$, and $CNT_{750°C}$ nanocomposites are attributable to several parameters, including carbon purity, length and diameter of CNTs, crystallinity of CNTs, states of dispersion within the PVDF matrix, etc. [7, 19]. The carbon purity for $CNT_{550°C}$, $CNT_{650°C}$, and $CNT_{750°C}$ were 43.6%, 85.4%, and 72.7%, respectively. Therefore, for a given filler loading incorporated within the PVDF matrix, $CNT_{650°C}$ had higher amount of CNTs, while for $CNT_{550°C}$, there was a huge amount of catalyst particles not contributing to the conductive network formation.

Theoretical and experimental studies showed well-dispersed CNTs with higher aspect ratio (larger length and smaller diameter) have lower percolation threshold, better electrical conductivity and EMI shielding. Smaller diameter signifies higher interacting surface area per mass of CNTs, and CNTs with larger length have more likelihoods to be in contact with each other. In addition, CPNs with better state of CNT dispersion present enhanced conductive network [49, 50]. Higher carbon purity and superior dispersion state of $CNT_{650°C}$ within the PVDF matrix coupled with its smaller diameter compared to $CNT_{550°C}$ and $CNT_{750°C}$ contributed to its superior electrical behavior. For comparison of $CNT_{550°C}$ and $CNT_{750°C}$ nanocomposites, it seems that smaller agglomerate area ratio along with smaller diameter of $CNT_{550°C}$ overshadowed its lower carbon purity and smaller length compared to $CNT_{750°C}$ and therefore, $CNT_{550°C}$ nanocomposites exhibited lower percolation threshold than their $CNT_{750°C}$ counterparts.

Figure 8(b) shows EMI SE of the generated nanocomposites as a function of CNT content. Despite having very high powder conductivity, both $CNT_{850°C}$ and $CNT_{950°C}$ nanocomposites presented SE very close to pure PVDF. $CNT_{650°C}$ nanocomposites showed SE far away superior to the other synthesis temperatures. These results are consistent with the conductivity data and reveal the remarkable impact of synthesis temperature on EMI shielding of CPNs. EMI SE of pure PVDF was 0.3dB, which increased to 8.9 and 20.3dB for $CNT_{650°C}$ nanocomposites with 1.0 and 3.5wt% loading, respectively. However, for instance, EMI SE of $CNT_{550°C}$ nanocomposite was 1.0 and 4.2dB for 1.0 and 3.5wt% CNT content, respectively. Table 4 compares EMI SE of $CNT_{650°C}$ nanocomposites developed in the current study with the literature, endorsing the high quality of synthesized $CNT_{650°C}$. It is worth noting that SE results obtained for $CNT_{650°C}$ nanocomposites were very close to the results acquired for commercial CNT (NC7000™, Nanocyl, Belgium) nanocomposites prepared with the same technique in our lab.

*Corresponding authors. Email: u.sundararaj@ucalgary.ca (Uttandaraman Sundararaj) and arjmand64@yahoo.com (Mohammad Arjmand)

Table 4: Comparison between SE of $CNT_{650°C}$ nanocomposite and polymer/CNT nanocomposite data from literature.

Polymer	Thickness (mm)	Loading	SE (dB)	Mixing Technique	Ref.
PVDF[1]	2	3% wt	10	Solution Mixing	[51]
PMMA[2]	2.54	3% wt	12	Solution Mixing	[52]
PVDF	0.9	3% wt	23	Solution Mixing	[53]
PVDF	2	5% wt	14	Melt Mixing	[54]
WPU[3]	2.3	76.2% wt	23	Freeze Cooling	[55]
PTT[4]	2	4.76 % vol	22	Melt Mixing	[56]
PP[5]	2.8	5% vol	24	Melt mixing	[57]
ABS[6]	1.1	15% wt	50	Solution Mixing	[58]
PC[7]	1.85	5% wt	25	Melt Mixing	[59]
PS[8]	2	20% wt	60	Melt Mixing	[60]
PS	2	7% wt	20	Solution mixing	[61]
PU[9]	2	20 wt%	17	Solution Mixing	[62]
PMMA	60-165 μm	40 wt%	27	Solution Mixing	[63]
PVDF	1.1	3.5 wt %	20.3	Melt Mixing	**This Work**

[1] Polyvinylidene fluoride; [2] Poly(methyl methacrylate); [3] Waterborne polyurethane; [4] Polytrimethylene terephthalate; [5] Polypropylene; [6] Acrylonitrile butadiene styrene; [7] Polycarbonates; [8] Polystyrene; [9] Polyurethane

*Corresponding authors. Email: u.sundararaj@ucalgary.ca (Uttandaraman Sundararaj) and arjmand64@yahoo.com (Mohammad Arjmand)

Two main mechanisms play role in EMI shielding, namely reflection and absorption [64, 65]. When an EM wave hits a conductive shield, a portion of the EM wave is reflected off the shield owing to interaction with the surface free charge carriers and a portion penetrates through the shield with its energy dissipated via absorption. Shielding by reflection for a conductive material is proportional to $\frac{\sigma}{\mu}$, where σ is electrical conductivity and μ is the magnetic permeability. Shielding by absorption for a conductive material is proportional to $\sigma \cdot \mu$, i.e., materials with high conductivity and high magnetic permeability attenuate EM wave efficiently. It is worth noting that the employed CNTs are non-magnetic; therefore, they mainly attenuate EM wave due to their high electrical conductivity.

To achieve an in-depth insight into the reasons behind superior EMI SE of $CNT_{650°C}$ nanocomposites compared to the others, shielding by reflection, shielding by absorption and dielectric properties of the developed nanocomposites as a function of CNT loading were investigated (Figure 9). The results unveiled that $CNT_{650°C}$ nanocomposites had higher both reflection and absorption compared to the other synthesis temperatures. It is also observed that the difference in shielding by absorption of $CNT_{650°C}$ nanocomposites and the other nanocomposites was much higher than shielding by reflection. For instance, for $CNT_{550°C}$ and $CNT_{650°C}$ nanocomposites with 3.5wt% loading, the shielding by reflection was 1.7dB and 4.4dB, whereas the shielding by absorption was 2.4dB and 15.8dB, respectively. Hence, it can be said that for $CNT_{650°C}$ nanocomposites, absorption played the role of the dominant mechanism, as shielding by absorption was intensely higher than shielding by reflection.

As mentioned in the previous section, shielding by reflection is commensurate with the conductivity (number of free charge carriers). $CNT_{650°C}$, in spite of having lower powder conductivity compared to CNTs synthesized at higher temperatures, presented higher shielding by reflection. This can be attributed to higher carbon purity, lower diameter, and better dispersion state of $CNT_{650°C}$, providing more interacting surface area projected to the incident EM wave compared to the other synthesis temperatures.

The absorption mechanism in CPNs is more sophisticated than that in conductive monolithic materials owing to their heterogeneous structure [66]. The physical structure of CNTs and level of formation of conductive network are the key parameters affecting the absorption mechanism [7]. Shielding by absorption in CPNs originates from Ohmic loss, represented by imaginary permittivity, and polarization loss, represented by real permittivity. Ohmic loss arises from the dissipation of energy by free electrons moving

*Corresponding authors. Email: u.sundararaj@ucalgary.ca (Uttandaraman Sundararaj) and arjmand64@yahoo.com (Mohammad Arjmand)

in phase with the applied electric field through conduction, hopping, and tunneling mechanisms [67]. Polarization loss originates from the energy required to reorient dipoles in each half cycle of alternating field. Over the X-band frequency range, the only probable polarization mechanisms are space polarization within CNTs and electronic polarization of the PVDF matrix [13, 68].

As illustrated in Figure 9(c-d), $CNT_{650°C}$ nanocomposites had a significantly higher imaginary permittivity and real permittivity compared to the other nanocomposites. For instance, at 3.5 wt% the imaginary permittivity of $CNT_{650°C}$ nanocomposites was 51.1, which was considerably higher than that of $CNT_{550°C}$ nanocomposite, i.e. 2.7. Several parameters could play roles in the higher imaginary permittivity of $CNT_{650°C}$ nanocomposites. As observed in the percolation curves (Figure 8(a)), $CNT_{650°C}$ nanocomposites had lower percolation threshold than the other nanocomposites. This signifies enhanced conductive network formation, facilitating the free charge carriers with more mean free paths to go through in each half cycle of the alternating field, thereby leading to enhanced absorption [60]. Low diameter, high carbon purity, and good dispersion state of $CNT_{650°C}$ significantly enhanced formation of conductive network formation in $CNT_{650°C}$ nanocomposite. Furthermore, CNT nanocomposites can be considered as a pool of nanocapacitors, with CNTs acting as nanoelectrodes and the PVDF matrix as nanodielectric [20]. In fact, in a CNT nanocomposite, there are many CNTs approaching each other but do not be connected. At enhanced conductive network formation, the likelihood of CNTs being in close contiguity is higher, nanodielectric thickness is smaller, and thus the applied electric field in nanocapacitor structures is higher. This reasoned higher real permittivity and polarization loss in $CNT_{650°C}$ nanocomposites.

Kuzhir et al. [69] and Shuba et al. [70] showed that the effective mass of CNTs involved in EMI shielding is much lower than the real mass due to screening of the inner shells of CNTs at K-band and lower frequencies. Accordingly, CNTs with higher aspect ratio are preferred as they experience less screening effect. They also showed that enhanced level of conductive network shifts CNTs to the dynamical regime by diminishing the depolarization effect on the outer shell. In the dynamical regime, the screening effect in CNTs is weak and EM wave penetrates deeper inside CNTs; thus, the greater number of CNT shells participates in shielding. Therefore, we can claim that low diameter and enhanced conductive network of $CNT_{650°C}$ nanocomposite contributed to higher involvement of CNT inner shells in EMI shielding, and thus assisted to higher energy dissipation.

*Corresponding authors. Email: u.sundararaj@ucalgary.ca (Uttandaraman Sundararaj) and arjmand64@yahoo.com (Mohammad Arjmand)
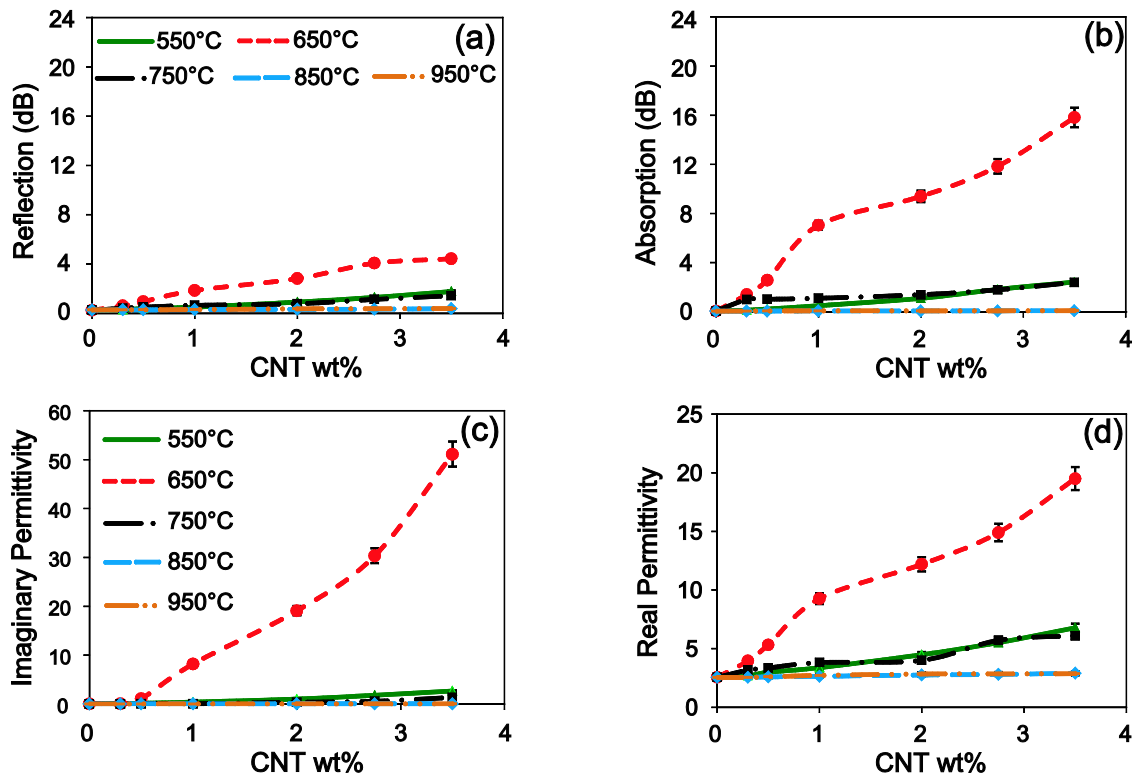
Figure 9: (a) Shielding by reflection, (b) shielding by absorption, (c) imaginary permittivity and (d) real permittivity of CNT/PVDF nanocomposites made at different synthesis temperatures as a function of CNT content.

4. Conclusions

*Corresponding authors. Email: u.sundararaj@ucalgary.ca (Uttandaraman Sundararaj) and arjmand64@yahoo.com (Mohammad Arjmand)

This study revealed that synthesis temperature has a tremendous impact on the morphology of CNTs and consequently morphological, rheological and electrical properties of their polymeric nanocomposites. Our study revealed that 650°C was the optimum temperature to develop CNTs and nanocomposites with far superior structural and electrical properties. We found that the nanocomposites made with $CNT_{650°C}$ had significantly lower percolation threshold and higher EMI SE than the other synthesis temperatures (550°C, 750°C, 850°C and 950°C). It was also observed that, contrary to the ascending trend of the powder conductivity with the synthesis temperature, the nanocomposites made with $CNT_{850°C}$ and $CNT_{950°C}$ demonstrated an insulative behavior and a very low EMI SE spanning the whole concentration range.

In short, based on the broad spectrum of characterization techniques employed, superior electrical properties of $CNT_{650°C}$ nanocomposites were ascribed to a combination of high carbon purity, high aspect ratio, high crystallinity, and good microdispersion and nanodispersion states of CNTs within the PVDF matrix. Insulative nature of $CNT_{850°C}$ and $CNT_{950°C}$ nanocomposites at the investigated CNT contents was mostly ascribed to severe sintering of catalyst particles at these high temperatures.

Supporting Information. XRD, Raman, HRTEM, DSC and size distribution of CNT samples, XRD of catalyst

References

[1] F. Qin, C. Brosseau, A review and analysis of microwave absorption in polymer composites filled with carbonaceous particles, J. Appl. Phys., 111 (2012) 061301.

*Corresponding authors. Email: u.sundararaj@ucalgary.ca (Uttandaraman Sundararaj) and arjmand64@yahoo.com (Mohammad Arjmand)

[2] M. Arjmand, A.A. Moud, Y. Li, U. Sundararaj, Outstanding electromagnetic interference shielding of silver nanowires: comparison with carbon nanotubes, RSC Adv. 5 (2015) 56590-56598.

[3] W. Bauhofer, J.Z. Kovacs, A review and analysis of electrical percolation in carbon nanotube polymer composites, Compos. Sci. Technol. 69 (2009) 1486-1498.

[4] E.T. Thostenson, Z.F. Ren, T.W. Chou, Advances in the science and technology of carbon nanotubes and their composites: A review, Compos. Sci. Technol. 61 (2001) 1899-1912.

[5] J.-M. Thomassin, C. Jerome, T. Pardoenb, C. Bailly, H. Isabelle, C. Detrembleur, Polymer/carbon based composites as electromagnetic interference (EMI) shielding materials, Mater. Sci. Eng., R 74 (2013) 211-232.

[6] J.N. Coleman, S. Curran, A.B. Dalton, A.P. Davey, B. McCarthy, W. Blau, R.C. Barklie, Percolation-dominated conductivity in a conjugated-polymer-carbon-nanotube composite, Phys. Rev. B 58 (1998) R7492-R7495.

[7] M. Arjmand, K. Chizari, B. Krause, P. Pötschke, U. Sundararaj, Effect of synthesis catalyst on structure of nitrogen-doped carbon nanotubes and electrical conductivity and electromagnetic interference shielding of their polymeric nanocomposites, Carbon 98 (2016) 358-372.

[8] B. Krause, M. Ritschel, C. Täschner, S. Oswald, W. Gruner, A. Leonhardt, P. Pötschke, Comparison of nanotubes produced by fixed bed and aerosol-CVD methods and their electrical percolation behaviour in melt mixed polyamide 6.6 composites, Compos. Sci. Technol. 70 (2010) 151-160.

[9] C. Mattevi, C.T. Wirth, S. Hofmann, R. Blume, M. Cantoro, C. Ducati, C. Cepek, A. Knop-Gericke, S. Milne, C. Castellarin-Cudia, S. Dolafi, A. Goldoni, R. Schloegl, J. Robertson, In-situ X-ray photoelectron spectroscopy study of catalyst-support interactions and growth of carbon nanotube forests, J. Phys. Chem. C 112 (2008) 12207-12213.

[10] B. Louis, G. Gulino, R. Vieira, J. Amadou, T. Dintzer, S. Galvagno, G. Centi, M.J. Ledoux, C. Pham-Huu, High yield synthesis of multi-walled carbon nanotubes by catalytic decomposition of ethane over iron supported on alumina catalyst, Catal. Today 102–103 (2005) 23-28.

[11] K.A. Shah, B.A. Tali, Synthesis of carbon nanotubes by catalytic chemical vapour deposition: A review on carbon sources, catalysts and substrates, Mater. Sci. Semicond. Process. 41 (2016) 67-82.

*Corresponding authors. Email: u.sundararaj@ucalgary.ca (Uttandaraman Sundararaj) and arjmand64@yahoo.com (Mohammad Arjmand)

[12] K. Chizari, A. Vena, L. Laureritius, U. Sundararaj, The effect of temperature on the morphology and chemical surface properties of nitrogen-doped carbon nanotubes, Carbon, 68 (2014) 369-379.

[13] M. Arjmand, U. Sundararaj, Effects of nitrogen doping on X-band dielectric properties of carbon nanotube/polymer nanocomposites, ACS Appl. Mater. Interfaces (2015) 17844-17850.

[14] J.K. Yuan, S.H. Yao, Z.M. Dang, A. Sylvestre, M. Genestoux, J.B. Bai, Giant dielectric permittivity nanocomposites: realizing true potential of pristine carbon nanotubes in polyvinylidene fluoride matrix through an enhanced interfacial interaction, J. Phys. Chem. C 115 (2011) 5515-5521.

[15] Z.M. Dang, S.H. Yao, J.K. Yuan, J.B. Bai, Tailored dielectric properties based on microstructure change in $BaTiO_3$-carbon nanotube/polyvinylidene fluoride three-phase nanocomposites, J. Phys. Chem. C 114 (2010) 13204-13209.

[16] V. Bhingardive, M. Sharma, S. Suwas, G. Madras, S. Bose, Polyvinylidene fluoride based lightweight and corrosion resistant electromagnetic shielding materials, RSC Adv. 5 (2015) 35909-35916.

[17] H. Gargama, A.K. Thakur, S.K. Chaturvedi, Polyvinylidene fluoride/nanocrystalline iron composite materials for EMI shielding and absorption applications, J. Alloys Compd. 654 (2016) 209-215.

[18] B. Krause, R. Boldt, L. Häußler, P. Pötschke, Ultralow percolation threshold in polyamide 6.6/MWCNT composites, Compos. Sci. Technol. 114 (2015) 119-125.

[19] M. Arjmand, U. Sundararaj, Electromagnetic interference shielding of nitrogen-doped and undoped carbon nanotube/polyvinylidene fluoride nanocomposites: A comparative study, Compos. Sci. Technol. 118 (2015) 257-263.

[20] A. Ameli, M. Arjmand, P. Pötschke, B. Krause, U. Sundararaj, Effects of synthesis catalyst and temperature on broadband dielectric properties of nitrogen-doped carbon nanotube/polyvinylidene fluoride nanocomposites, Carbon 106 (2016) 260-278.

[21] W.B. Weir, Automatic measurement of complex dielectric constant and permeability at microwave frequencies, Proc. IEEE 62 (1974) 33-36.

*Corresponding authors. Email: u.sundararaj@ucalgary.ca (Uttandaraman Sundararaj) and arjmand64@yahoo.com (Mohammad Arjmand)

[22] A.M. Nicolson, G.F. Ross, Measurement of the intrinsic properties of materials by time-domain techniques, IEEE Trans. Instrum. Meas. 19 (1970) 377-382.

[23] M. Arjmand, M. Mahmoodi, S. Park, U. Sundararaj, An innovative method to reduce the energy loss of conductive filler/polymer composites for charge storage applications, Compos. Sci. Technol. 78 (2013) 24-29.

[24] Y. Huang, N. Li, Y.F. Ma, D. Feng, F.F. Li, X.B. He, X. Lin, H.J. Gao, Y.S. Chen, The influence of single-walled carbon nanotube structure on the electromagnetic interference shielding efficiency of its epoxy composites, Carbon 45 (2007) 1614-1621.

[25] A.C. Ferrari, J. Robertson, Interpretation of Raman spectra of disordered and amorphous carbon, Phys. Rev. B 61 (2000) 14095-14107.

[26] K. Jeon, S. Warnock, C. Ruiz-Orta, A. Kismarahardja, J. Brooks, R.G. Alamo, Role of matrix crystallinity in carbon nanotube dispersion and electrical conductivity of iPP-based nanocomposites, J. Polym. Sci., Part B: Polym. Phys. 48 (2010) 2084-2096.

[27] S. Sadeghi, A. Zehtab Yazdi, U. Sundararaj, Controlling short-range interactions by tuning surface chemistry in HDPE/graphene nanoribbon nanocomposites, J. Phys. Chem. B 119 (2015) 11867-11878.

[28] J. Sprakel, S.B. Lindström, T.E. Kodger, D.A. Weitz, Stress enhancement in the delayed yielding of colloidal gels, Phys. Rev. Lett. 106 (2011) 248303.

[29] M. Laurati, S. Egelhaaf, G. Petekidis, Nonlinear rheology of colloidal gels with intermediate volume fraction, J. Rheol. 55 (2011) 673-706.

[30] N. Koumakis, G. Petekidis, Two step yielding in attractive colloids: transition from gels to attractive glasses, Soft Matter 7 (2011) 2456-2470.

[31] J. Kim, D. Merger, M. Wilhelm, M.E. Helgeson, Microstructure and nonlinear signatures of yielding in a heterogeneous colloidal gel under large amplitude oscillatory shear, J. Rheol. 58 (2014) 1359-1390.

[32] Z. Shao, A.S. Negi, C.O. Osuji, Role of interparticle attraction in the yielding response of microgel suspensions, Soft Matter 9 (2013) 5492-5500.

*Corresponding authors. Email: u.sundararaj@ucalgary.ca (Uttandaraman Sundararaj) and arjmand64@yahoo.com (Mohammad Arjmand)

[33] J.P. Segovia-Gutiérrez, C.L.a. Berli, J. de Vicente, Nonlinear viscoelasticity and two-step yielding in magnetorheology: A colloidal gel approach to understand the effect of particle concentration, J. Rheol. 56 (2012) 1429-1448.

[34] H.J. Walls, S.B. Caines, A.M. Sanchez, S.a. Khan, Yield stress and wall slip phenomena in colloidal silica gels, J. Rheol. 47 (2003) 847-868.

[35] M.A. Fardin, C. Perge, L. Casanellas, T. Hollis, N. Taberlet, J. Ortin, S. Lerouge, S. Manneville, Flow instabilities in large amplitude oscillatory shear: a cautionary tale, Rheol. Acta 53 (2014) 885-898.

[36] L.C. Hsiao, R.S. Newman, S.C. Glotzer, M.J. Solomon, Role of isostaticity and load-bearing microstructure in the elasticity of yielded colloidal gels, PNAS 109 (2012) 16029-16034.

[37] H. Wu, M. Morbidelli, A model relating structure of colloidal gels to their elastic properties, Langmuir, 17 (2001) 1030-1036.

[38] H.K. Chan, A. Mohraz, Two-step yielding and directional strain-induced strengthening in dilute colloidal gels, Phys. Rev. E 85 (2012) 041403.

[39] Y.L. Yang, M.C. Gupta, K.L. Dudley, R.W. Lawrence, A comparative study of EMI shielding properties of carbon nanofiber and multi-walled carbon nanotube filled polymer composites, J. Nanosci. Nanotechnol. 5 (2005) 927-931.

[40] M. Weber, M.R. Kamal, Estimation of the volume resistivity of electrically conductive composites, Polym. Compos. 18 (1997) 711-725.

[41] C.-C.M. Ma, Y.-L. Huang, H.-C. Kuan, Y.-S. Chiu, Preparation and electromagnetic interference shielding characteristics of novel carbon-nanotube/siloxane/poly-(urea urethane) nanocomposites, J. Polym. Sci., Part B: Polym. Phys. 43 (2005) 345-358.

[42] R. Ram, M. Rahaman, D. Khastgir, Electrical properties of polyvinylidene fluoride (PVDF)/multi-walled carbon nanotube (MWCNT) semi-transparent composites: Modelling of DC conductivity, Composites, Part A, 69 (2015) 30-39.

[43] V. Eswaraiah, V. Sankaranarayanan, S. Ramaprabhu, Inorganic nanotubes reinforced polyvinylidene fluoride composites as low-cost electromagnetic interference shielding materials, Nanoscale Res. Lett. 6 (2011) 1-11.

*Corresponding authors. Email: u.sundararaj@ucalgary.ca (Uttandaraman Sundararaj) and arjmand64@yahoo.com (Mohammad Arjmand)

[44] K. Ke, P. Pötschke, D. Jehnichen, D. Fischer, B. Voit, Achieving β-phase poly (vinylidene fluoride) from melt cooling: effect of surface functionalized carbon nanotubes, Polymer 55 (2014) 611-619.

[45] G.R. Ruschau, S. Yoshikawa, R.E. Newnham, Resistivities of conductive composites, J. Appl. Phys. 72 (1992) 953-959.

[46] Z. Spitalsky, D. Tasis, K. Papagelis, C. Galiotis, Carbon nanotube-polymer composites: Chemistry, processing, mechanical and electrical properties, Prog. Polym. Sci. 35 (2010) 357-401.

[47] I. Balberg, C.H. Anderson, S. Alexander, N. Wagner, Excluded volume and its relation to the onset of percolation, Phys. Rev. B 30 (1984) 3933-3943.

[48] L. Onsager, The effects of shape on the interaction of colloidal particles, Ann. N.Y. Acad. Sci. 51 (1949) 627-659.

[49] J. Li, P.C. Ma, W.S. Chow, C.K. To, B.Z. Tang, J.K. Kim, Correlations between percolation threshold, dispersion state, and aspect ratio of carbon nanotubes, Adv. Funct. Mater. 17 (2007) 3207-3215.

[50] P.V. Kodgire, A.R. Bhattacharyya, S. Bose, N. Gupta, A.R. Kulkarni, A. Misra, Control of multiwall carbon nanotubes dispersion in polyamide6 matrix: An assessment through electrical conductivity, Chem. Phys. Lett. 432 (2006) 480-485.

[51] H. Wang, K. Zheng, X. Zhang, T. Du, C. Xiao, X. Ding, C. Bao, L. Chen, X. Tian, Segregated poly (vinylidene fluoride)/MWCNTs composites for high-performance electromagnetic interference shielding, Composites, Part A 90 (2016) 606-613.

[52] T. Kuang, L. Chang, F. Chen, Y. Sheng, D. Fu, X. Peng, Facile preparation of lightweight high-strength biodegradable polymer/multi-walled carbon nanotubes nanocomposite foams for electromagnetic interference shielding, Carbon 105 (2016) 305-313.

[53] B. Bhaskara Rao, N. Kale, B. Kothavale, S. Kale, Fabrication and evaluation of thin layer PVDF composites using MWCNT reinforcement: Mechanical, electrical and enhanced electromagnetic interference shielding properties, AIP Adv. 6 (2016) 065107.

[54] H. Wang, K. Zheng, X. Zhang, X. Ding, Z. Zhang, C. Bao, L. Guo, L. Chen, X. Tian, 3D network porous polymeric composites with outstanding electromagnetic interference shielding, Compos. Sci. Technol. 125 (2016) 22-29.
*Corresponding authors. Email: u.sundararaj@ucalgary.ca (Uttandaraman Sundararaj) and arjmand64@yahoo.com (Mohammad Arjmand)

[55] Z. Zeng, H. Jin, M. Chen, W. Li, L. Zhou, Z. Zhang, Lightweight and anisotropic porous MWCNT/WPU composites for ultrahigh performance electromagnetic interference shielding, Adv. Funct. Mater. 26 (2016) 303-310.

[56] A. Gupta, V. Choudhary, Electrical conductivity and shielding effectiveness of poly (trimethylene terephthalate)/multiwalled carbon nanotube composites, J. Mater. Sci. 46 (2011) 6416-6423.

[57] M.H. Al-Saleh, U. Sundararaj, Electromagnetic interference shielding mechanisms of CNT/polymer composites, Carbon 47 (2009) 1738-1746.

[58] M.H. Al-Saleh, W.H. Saadeh, U. Sundararaj, EMI shielding effectiveness of carbon based nanostructured polymeric materials: A comparative study, Carbon 60 (2013) 146-156.

[59] M. Arjmand, M. Mahmoodi, G.A. Gelves, S. Park, U. Sundararaj, Electrical and electromagnetic interference shielding properties of flow-induced oriented carbon nanotubes in polycarbonate, Carbon, 49 (2011) 3430-3440.

[60] M. Arjmand, T. Apperley, M. Okoniewski, U. Sundararaj, Comparative study of electromagnetic interference shielding properties of injection molded versus compression molded multi-walled carbon nanotube/polystyrene composites, Carbon 50 (2012) 5126-5134.

[61] Y. Yang, M.C. Gupta, K.L. Dudley, R.W. Lawrence, Novel carbon nanotube-polystyrene foam composites for electromagnetic interference shielding, Nano Lett. 5 (2005) 2131-2134.

[62] Z. Liu, G. Bai, Y. Huang, Y. Ma, F. Du, F. Li, T. Guo, Y. Chen, Reflection and absorption contributions to the electromagnetic interference shielding of single-walled carbon nanotube/polyurethane composites, Carbon 45 (2007) 821-827.

[63] H. Kim, K. Kim, C. Lee, J. Joo, S. Cho, H. Yoon, D. Pejaković, J.-W. Yoo, A. Epstein, Electrical conductivity and electromagnetic interference shielding of multiwalled carbon nanotube composites containing Fe catalyst, Appl. Phys. Lett. 84 (2004) 589-591.

[64] K.L. Kaiser, Electromagnetic Shielding, CRC Press, Boca Raton, 2006.

[65] C.R. Paul, Introduction to Electromagnetic Compatibility, John Wiley & Sons, Inc., New Jersey, 2006.

*Corresponding authors. Email: u.sundararaj@ucalgary.ca (Uttandaraman Sundararaj) and arjmand64@yahoo.com (Mohammad Arjmand)

[66] P.A.M. Steeman, J.V. Turnhout, Dielectric properties of inhomogeneous media, in: F. Kremer, A. Schöndals (Eds.), Broadband Dielectric Spectrosocpy, Springer-Verlag, Berlin, 2003, pp. 495-522.

[67] I. Balberg, Tunneling and nonuniversal conductivity in composite materials, Phys. Rev. Lett. 59 (1987) 1305-1308.

[68] M. Arjmand, Electrical conductivity, electromagnetic interference shielding and dielectric properties of multi-walled carbon nanotube/polymer composites, PhD Thesis, University of Calgary, 2014.

[69] P.P. Kuzhir, A.G. Paddubskaya, M.V. Shuba, S.A. Maksimenko, A. Celzard, V. Fierro, G. Amaral-Labat, A. Pizzi, G. Valušis, J. Macutkevic, Electromagnetic shielding efficiency in Ka-band: carbon foam versus epoxy/carbon nanotube composites, J. Nanophoton. 6 (2012) 061715-061715.

[70] M.V. Shuba, A.V. Melnikov, A.G. Paddubskaya, P.P. Kuzhir, S.A. Maksimenko, C. Thomsen, Role of finite-size effects in the microwave and subterahertz electromagnetic response of a multiwall carbon-nanotube-based composite: Theory and interpretation of experiments, Phys. Rev. B 88 (2013) 045436.

*Corresponding authors. Email: u.sundararaj@ucalgary.ca (Uttandaraman Sundararaj) and arjmand64@yahoo.com (Mohammad Arjmand)

Supporting Information for

Impact of Synthesis Temperature on Morphology, Rheology and Electromagnetic Interference Shielding of CVD-Grown Carbon Nanotube/Polyvinylidene Fluoride Nanocomposites

Seyyed Alireza Mirkhani[a,†], Mohammad Arjmand[a,†], Soheil Sadeghi[a], Beate Krause[b], Petra Pötschke[b], Uttandaraman Sundararaj[a,*]

[a]Department of Chemical and Petroleum Engineering, University of Calgary, Calgary, Canada

[b]Department of Functional Nanocomposites and Blends, Leibniz Institute of Polymer Research Dresden (IPF), Dresden, Germany

Contents for Supplementary Materials

*Corresponding authors. Email: u.sundararaj@ucalgary.ca (Uttandaraman Sundararaj) and arjmand64@yahoo.com (Mohammad Arjmand)

Experimental

1.1. X-ray diffraction (XRD)

The XRD analysis of the calcinated and reduced catalysts and CNTs was performed with a Rigaku ULTIMA III X-ray diffractometer with Cu K-alpha radiation as the X-ray source. The sweeping range of XRD scan was set to $2\theta = 10–90$ degrees using a 0.02 degree step and a counting time of 1 degree per minute at 40kV and 44mA.

1.2.   Transmission electron microscopy of CNTs

High-resolution transmission electron microscopy (HRTEM) was used to investigate the morphology of synthesized CNTs. HRTEM was performed on a Tecnai TF20 G2 FEG-TEM (FEI, Hillsboro, Oregon, USA) at 200kV acceleration voltage with a standard single-tilt holder. The images were captured with a Gatan UltraScan 4000 CCD camera (Gatan, Pleasanton, California, USA) at 2048×2048 pixels. For the HRTEM, less than 1.0mg of the CNT powder was suspended in 10mL ethanol and bath sonicated for 15min. A drop of the suspension was mounted on the carbon side of a standard TEM grid covered with a ~ 40nm holey carbon film (EMS, Hatfield, Pennsylvania, USA). Measurement of the geometrical dimensions of CNTs was performed for more than 150 individual ones using the MeasureIT software (Olympus Soft Imaging Solutions GmbH).

1.3.   Raman spectroscopy

The structural defects of CNTs were inspected using Raman spectroscopy. The powder samples of CNTs were placed on a clean gold substrate and analyzed. The Raman spectra were recorded with a Renishaw inVia Raman microscope. Excitation was provided by the radiation of an argon-ion laser beam with 514nm wavelength. All spectra were collected with a $5\times$ objective.

1.4.   Differential scanning calorimetry (DSC)

DSC on the compression-molded samples was used to quantify the effect of synthesized CNTs on the overall PVDF crystallinity, and the nucleation effects. Heating-Cooling-Heating cycles were carried out at 10K/min in N_2 atmosphere using a DSC Q100 instrument (TA Instruments). Crystallinity was calculated from the heat capacity in the second heating run, corrected for polymer content, and using the value for 100% crystallinity of PVDF, i.e. 104.7J/g [1-2]. The extrapolated onset temperature of crystallization $T_{c,0}$ and the maximum crystallization $T_{c,m}$ temperature were defined.

2.   Results and Discussion

2.1. XRD of catalyst and CNT

Figure S1 demonstrates the XRD patterns of the calcinated and reduced catalysts. It is observed that after the reduction stage the iron oxide peaks vanish, and only alumina peaks remain. Moreover, in the reduced catalyst a new peak appears, corresponding to metallic iron. XRD patterns confirm that the relatively high reduction temperature transformed almost all iron oxide into metallic iron.
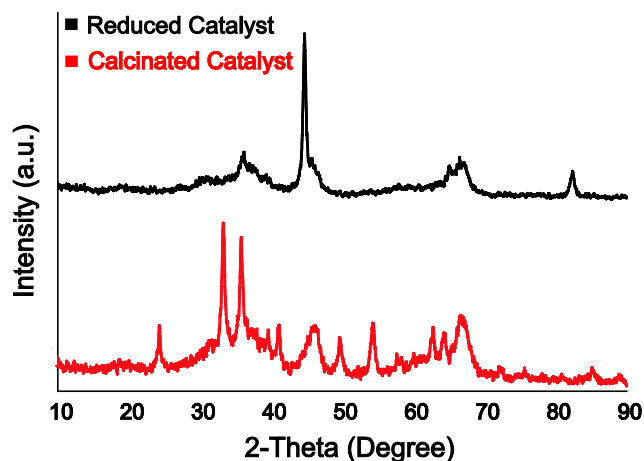
Figure S1: Comparison of XRD patterns of calcinated and reduced catalysts.

Figure S2 depicts the XRD patterns of synthesized CNTs. It is observed that there is a common sharp peak at 26° in all spectra, corresponding to (002) peak of graphitic structures. Qualitatively, XRD can also reveal invaluable information about the carbon purity of synthesized CNTs. As seen in Figure S2, the intensity of the peaks of iron catalyst at about 45° is minimum for $CNT_{650°C}$ and maximum for $CNT_{550°C}$, whereas the other types of CNTs showed intermediate values. These results confirm that 650°C led to maximum carbon purity and 550°C resulted in the lowest carbon purity.
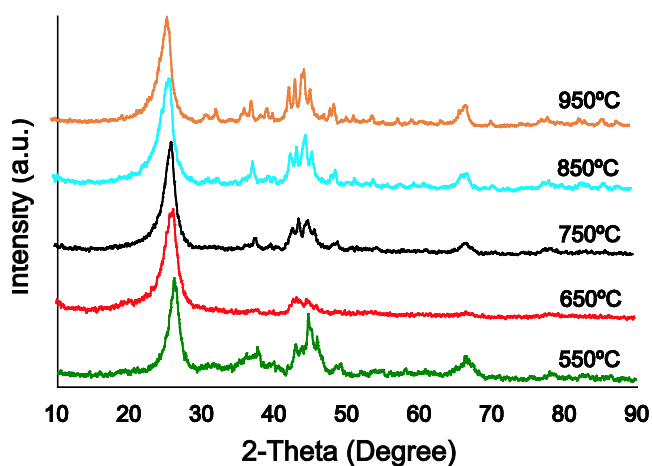
Figure S2: XRD analysis of CNT samples.

2.2. TEM of CNT

Figure S3 illustrates the typical TEM images of CNTs synthesized at various temperatures. We observed almost similar morphology for CNTs synthesized at 550℃, 650℃ and 750℃ (Figure S3a-c). CNTs synthesized at these three temperatures present a structure with relatively straight and parallel walls and a through internal channel; CNTs synthesized at 650℃ had a more crystalline structure though. Low-magnification TEM images (Figure 3f-h) revealed low, high and intermediate carbon purity for $CNT_{550℃}$, $CNT_{650℃}$, and $CNT_{750℃}$, respectively, in line with SEM and TGA results. TEM micrographs revealed a different morphology for CNTs synthesized at 850℃ and 950℃ compared to the other temperatures. $CNT_{850℃}$ and $CNT_{950℃}$ had a relatively consistent inner and outer diameter, and the same number of walls throughout the channel with an ordered crystal structure, due to high synthesis temperature. However, we interestingly observed a thick layer of non-graphitic carbonaceous material encapsulating synthesized CNTs (Figure S3d-e). Low-magnification TEM images of $CNT_{850℃}$ and $CNT_{950℃}$ demonstrate the sintering and coalescence of catalyst particles, leading to formation of thermal-resistant carbonaceous material on the surface of catalyst, besides CNTs (Figure S3i-j). This is another proof of formation of highly thermal-resistant material at 850℃ and 950℃, in addition to TGA, SEM and powder conductivity.
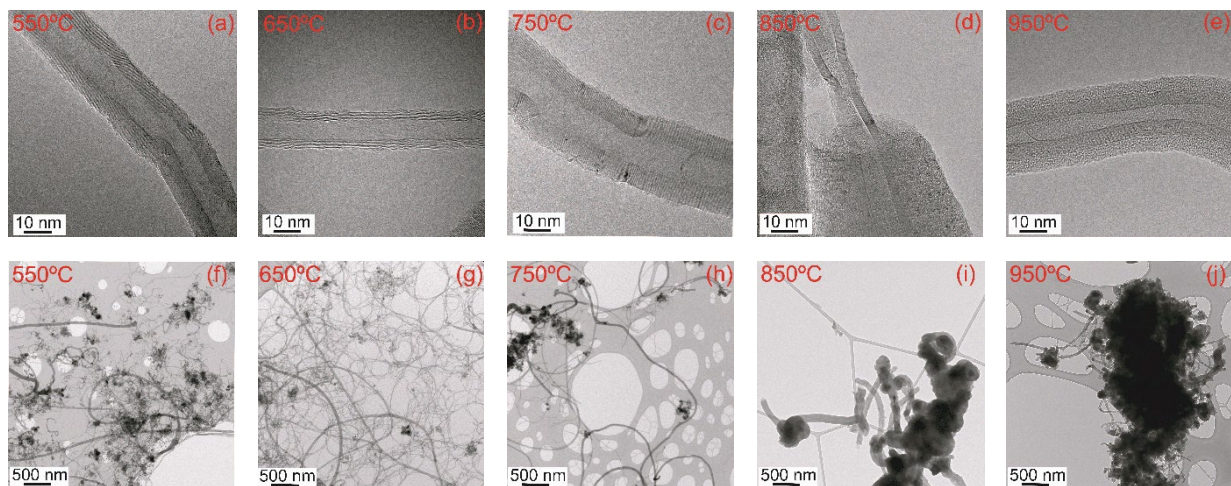

Figure S3: (a-e) High-magnification and (f-j) low-magnification TEM micrographs of CNTs synthesized at 550℃, 650℃, 750℃, 850℃ and 950℃.
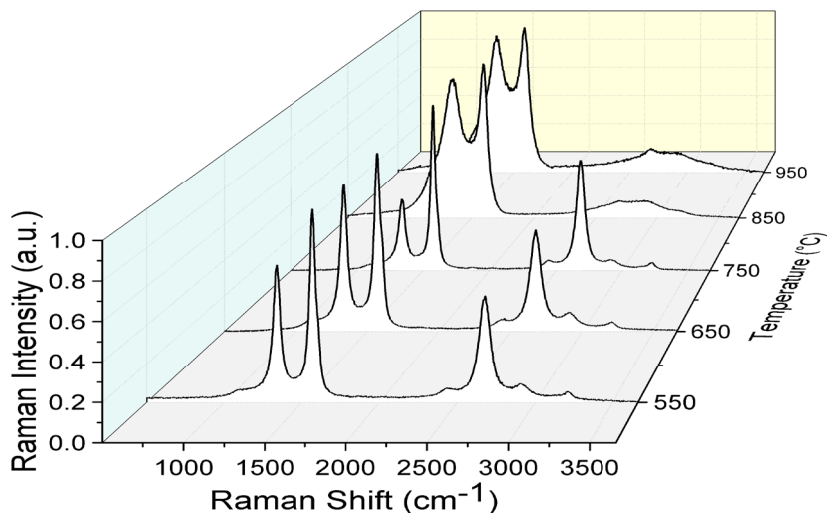
2.3. Raman spectroscopy

Figure S4: Raman spectra of CNT samples synthesized at different temperatures.

2.4. *Size distribution of CNTs*

Figure S5 depicts the length and diameter distribution of CNTs synthesized at 550℃, 650℃ and 750℃. It is worth noting that we could not find enough CNTs at 850℃ and 950℃ to provide histograms for length and diameter distribution. This is due to sintering and coalescence of catalysts particles, hindering the formation of CNTs. The average values of length and diameter of CNTs are presented in Figure 3(a). CNTs synthesized at 550℃, 650℃ and 750℃ showed average diameters of 21.6nm, 14.7nm and 29.4nm and lengths of 1.29μm, 0.68μm and 1.37μm, respectively. The interesting point is that $CNT_{650℃}$ presented a much narrower length and diameter distribution compared to the other two temperatures. For instance, the maximum diameter observed for $CNT_{650℃}$ is about 40nm, whereas CNTs up to 90nm diameter were observed at 550℃ and 750℃. This says that $CNT_{650℃}$ had larger surface area compared to the other temperatures, contributing to enhanced electrical properties. In terms of length, CNTs as long as 16μm and 35 μm were observed for $CNT_{550℃}$ and $CNT_{750℃}$, respectively, whereas CNTs synthesized at 650℃ were no longer than 4.0μm.
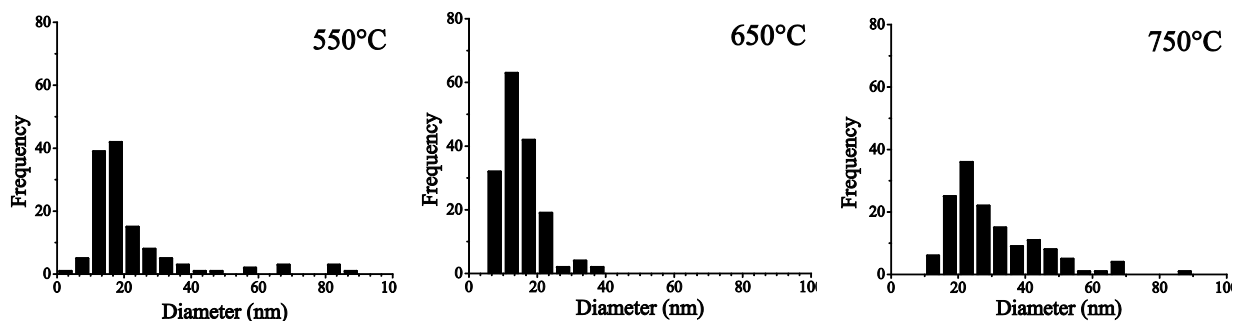

40
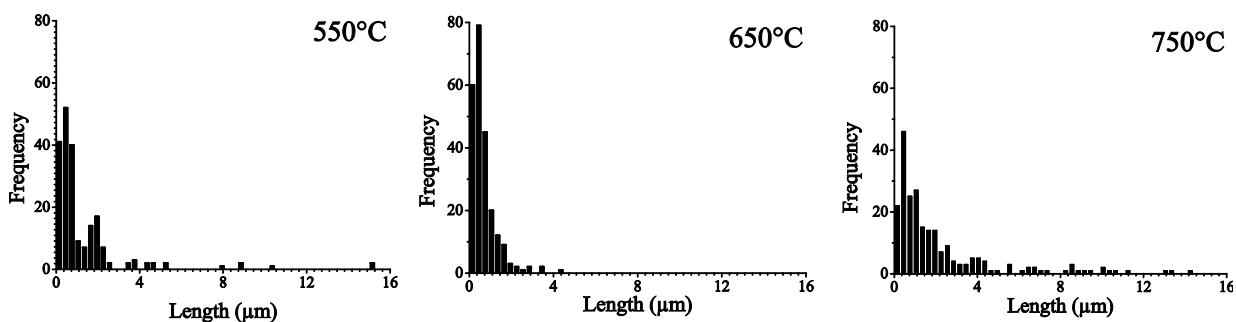
Figure S5: Length and diameter distribution of CNTs synthesized at 550°C, 650°C and 750°C.

2.5. DSC

DSC was executed to evaluate to the influence of synthesized nanofillers on crystallinity and the crystallization behavior of the PVDF nanocomposites. It is known that the matrix crystallinity may influence the composite's electrical properties [3]. As the changes in the onset and peak crystallization temperatures and crystallinity are related to the amount and chemical characteristics of surface available for crystallization, various CNT structures may lead to differences. Figure S6 shows the cooling scan of the DSC measurements, illustrating the nucleating effect of all CNTs. Compared to pure PVDF, the extrapolated onset and peak crystallization temperatures of the nanocomposites were shifted on average up to 9K and 16K, respectively, to higher values. The highest nucleating effect was observed for $CNT_{650°C}$, followed by $CNT_{750°C}$ and $CNT_{550°C}$. However, the overall crystallinity increased only slightly from 49.5% for pure PVDF to max. 53.5% for $CNT_{750°C}$. The results illustrate that changes in the electrical behavior were not due to different PVDF matrix crystallinity.
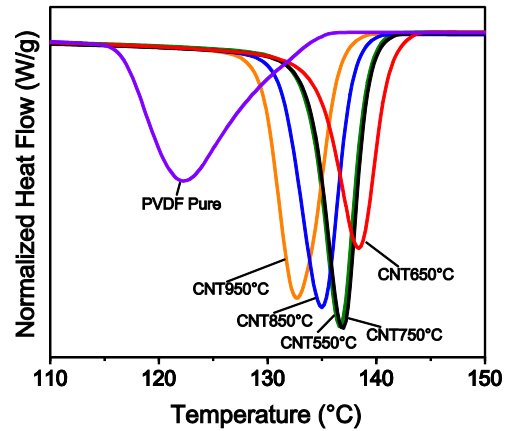
Figure S6: DSC cooling runs of pure PVDF and 2.0wt% CNT/PVDF nanocomposites corresponding to different CNT synthesis temperatures.

3. References

1.   U. Gaur, B.B. Wunderlich, B. Wunderlich, Heat capacity and other thermodynamic properties of linear macromolecules. vii. Other carbon backbone polymers, J. Phys. Chem. Ref. Data 12 (1983) 29-63.

2.   B. Wunderlich, Thermal Analysis, Academic Press, Boston, 1990.

3.   K. Jeon, S. Warnock, C. Ruiz-Orta, A. Kismarahardja, J. Brooks, R.G. Alamo, Role of matrix crystallinity in carbon nanotube dispersion and electrical conductivity of iPP-based nanocomposites. J. Polym. Sci., Part B: Polym. Phys. 48 (2010) 2084-2096.